ULTRALUMINOUS X-RAY SOURCES IN ARP 147

The Astrophysical Journal, 721:1348–1355, 2010 October 1 doi:10.1088/0004-637X/721/2/1348

ULTRALUMINOUS X-RAY SOURCES IN ARP 147

S. Rappaport[1], A. Levine[2], D. Pooley[3], and B. Steinhorn[1]
[1] 37-602B, M.I.T. Department of Physics and Kavli Institute for Astrophysics and Space Research, 70 Vassar Street, Cambridge, MA 02139, USA; sar@mit.edu
[2] 37-575 M.I.T. Kavli Institute for Astrophysics and Space Research, 70 Vassar Street, Cambridge, MA 02139, USA; aml@space.mit.edu
[3] Eureka Scientific, 5248 Valley View Road El Sobrante, CA 94803-3435, USA; pooley@gmail.com
Received 2010 July 16; accepted 2010 August 2; published 2010 September 9

ABSTRACT

The *Chandra X-Ray Observatory* was used to image the collisional ring galaxy Arp 147 for 42 ks. We detect nine X-ray sources with luminosities in the range of (1.4–7) $\times$ 10^{39} erg s^{-1} (assuming that the sources emit isotropically) in or near the blue knots of star formation associated with the ring. A source with an X-ray luminosity of 1.4 $\times$ 10^{40} erg s^{-1} is detected in the nuclear region of the intruder galaxy. X-ray sources associated with a foreground star and a background quasar are used to improve the registration of the X-ray image with respect to *Hubble Space Telescope* (*HST*) high-resolution optical images. The intruder galaxy, which apparently contained little gas before the collision, shows no X-ray sources other than the one in the nuclear bulge which may be a poorly fed supermassive black hole. These observations confirm the conventional wisdom that collisions of gas-rich galaxies trigger large rates of star formation which, in turn, generate substantial numbers of X-ray sources, some of which have luminosities above the Eddington limit for accreting stellar-mass black holes (i.e., ultraluminous X-ray sources, "ULXs"). We also utilize archival *Spitzer* and *Galex* data to help constrain the current star formation rate in Arp 147 to $\sim$7 $M_\odot$ yr^{-1}. All of these results, coupled with binary evolution models for ULXs, allow us to tentatively conclude that the most intense star formation may have ended some 15 Myr in the past.

Key words: binaries: general – galaxies: individual (Arp 147) – galaxies: interactions – galaxies: nuclei – galaxies: starburst – galaxies: structure – stars: formation – stars: luminosity function, mass function – stars: neutron

1. INTRODUCTION

If one or both of a pair of colliding galaxies has a high gas content, the collision may trigger a spectacular burst of star formation like those seen in the Antennae (Whitmore & Schweizer 1995) and the Cartwheel (e.g., Higdon 1995; Amram et al. 1998). In the latter case, a smaller intruder galaxy passed through the disk of the progenitor spiral galaxy about (1.5–2) $\times$ 10^8 yr ago. This triggered a wave of star formation which has propagated radially outward at an effective speed of $\gtrsim$100 km s^{-1} and is apparent as a brilliant, expanding ring. The dynamics of this so-called collisional ring galaxy and other colliding galaxies, including examples that are remarkably similar in appearance to the Cartwheel, have been explored and understood at least in part through numerical simulations (see, e.g., Lynds & Toomre 1976; Toomre 1978; Gerber et al. 1992; Mihos & Hernquist 1994; Appleton & Struck 1996; Mapelli et al. 2008).

Many of the newly formed stars in a collision-induced ring or other star formation region will naturally constitute binary systems. Some fraction of the more massive stars in these binaries evolve rapidly to form conventional high-mass X-ray binaries (with neutron-star or stellar-mass black-hole accretors and $L_x \lesssim 10^{39}$ erg s^{-1}) that can be detected with *Chandra* out to distances of $\sim$50 Mpc (see, e.g., Fabbiano 2006). If the examples of the Antennae (Zezas & Fabbiano 2002) and the Cartwheel (Gao et al. 2003; Wolter et al. 2006) are representative, galaxy collisions also produce substantial numbers of ultraluminous X-ray sources ("ULXs") which are characterized by $L_x \gtrsim 10^{39}$ erg s^{-1}. The nature of the ULXs is unclear at present; they are likely to be binaries with black-hole accretors, but the accretors could be either of stellar mass and accreting at rates above the Eddington limit or of masses 1–2 orders of magnitude higher and be so-called intermediate-mass black holes ("IMBHs;" see, e.g., Colbert & Mushotzky 1999).

At the higher end of the ULX luminosity function, i.e., at $L_x \gtrsim 10^{40}$ erg s^{-1}, and especially as the inferred luminosities approach $\sim 10^{41}$ erg s^{-1} (e.g., ESO 243-49; Farrell et al. 2009; Godet et al. 2009), it becomes increasingly difficult to see how the requisite emission, even if somewhat beamed, could be produced around a stellar-mass black hole (see, e.g., Madhusudhan et al. 2008). By contrast, the X-ray luminosities of accreting IMBHs could easily exceed 10^{41} erg s^{-1} without violating the Eddington limit, but this explanation of ULXs is confronted by other serious problems. Portegies Zwart et al. (2004a), among others, have proposed that runaway star collisions in newly formed massive star clusters lead to the formation of supermassive stars (e.g., $\gtrsim$500 $M_\odot$) which, in turn, evolve to form IMBHs. The IMBHs must then capture massive stars into orbits where mass transfer will proceed at levels sufficient to produce the requisite X-ray emission. However, the evolution of supermassive stars is highly uncertain. For example, Yungelson et al. (2008) showed that such massive stars resulting from runaway collisions would likely ultimately be reduced to $\lesssim$150 $M_\odot$ due to wind mass loss. Moreover, the efficiency for producing the requisite numbers of IMBHs in the Cartwheel has been argued to be implausibly high (King 2004). IMBHs from Population III remnants are unlikely to show the requisite spatial coincidence with star formation regions exhibited by ULXs (cf. Krolik 2004). A better understanding of ULXs could shed much light on these issues and on the formation and evolution of very massive stars.

Since it appears that substantial numbers of ULXs are commonly found in collisional ring galaxies, it would seem like these would be good targets for *Chandra* observations. The "Atlas and Catalog of Collisional Ring Galaxies" (Madore et al. 2009) contains information on $\sim$104 collisional ring galaxies. While this atlas focuses on southern hemisphere objects, it also includes information on northern hemisphere collisional ring galaxies that are described in the literature including the Arp

peculiar galaxy catalogs (Arp 1966; Arp & Madore 1987). We find that only 4 of the ∼104 collisional ring galaxies have been observed by *Chandra*. One of these is the Cartwheel galaxy. The others are Arp 284, Arp 318, and AM 0644−741, but Arp 318 was observed at an off-axis angle of $> 4'$ so the existing data would not be useful in resolving individual point sources. Results from the observation of Arp 284 have been published by Smith et al. (2005) who report the detection of ∼7 ULXs, with two having $L_x \sim 10^{40}$ erg s^{-1}.

In 2009 July, we obtained *Chandra* observations of the well-known collisional ring galaxy Arp 147. An image of Arp 147 taken earlier with the WFPC2 on *Hubble Space Telescope* (*HST*) is shown in Figure 1(a). The object consists of the ring-like remnant of what was originally a gas-rich galaxy that likely underwent, according to Gerber et al. (1992), an off-center collision with an approximately equal-mass (∼1.8×10^{11} $M_\odot$) elliptical galaxy that passed "perpendicular through the disk about two radial scale lengths from the center." However, simulations of similar systems suggest that the mass of the intruder could be 2–3 times more massive than the ring (A. Toomre 2010, private communication). Hereafter, we refer to the ring-like structure exhibiting a high star formation rate (SFR; see, e.g., the blue knots in Figure 1(a)) as the "ring," and to the reddish neighbor galaxy, which also appears to have a tidally induced ring structure, as the "intruder." The maximum angular extents of the ring and the intruder galaxies are ∼18″–19″, and their recession velocities are 9415 and 9656 km s^{-1}, respectively. For a Hubble constant of $H_0 = 72$ km s^{-1} Mpc^{-1} (e.g., Freedman 2003), the distance to Arp 147 is ∼133 Mpc, and the corresponding physical size of the two objects is ∼12 kpc. Finally, we note that the reddish-pink region seen in the *HST* image on the south–southeast side of the ring is thought to be the nucleus of the original spiral galaxy which the intruder has tidally stretched into an apparently ring-like structure (e.g., Gerber et al. 1992).

In Section 2.1 of this work we describe the *Chandra* X-ray observations and the analysis of the data. The supplemental images from the *HST*, *Spitzer*, and *Galex* observatories are described in Sections 2.2–2.4. In Section 3, we present the results of the X-ray observations including a table that lists source locations, fluxes, luminosities, median photon energies, and power-law spectral indices. The "SFR" in the ring portion of Arp 147 is inferred from, and contrasted among, the *Spitzer* and *Galex* fluxes as well the number of luminous X-ray sources.

2. OBSERVATIONS

2.1. Chandra Observations

Arp 147 was observed with *Chandra* with the Advanced CCD Imaging Spectrometer (ACIS) at the focal plane. The data were taken in the timed-exposure mode with an integration time of 3.24 s per frame, and the telescope aim point was on the backside-illuminated S3 chip. A 24.5 ks exposure (ObsID 11280) was made on 2009 September 13 and an 18.0 ks exposure (ObsID 11887) was made on 2009 September 15 for a total exposure of 42.5 ks.

The data from the two observations were merged and were reprocessed without the pixel randomization that is included during standard processing. Reprocessing the data in this way slightly improves the point-spread function. An X-ray image was then formed from the events in the energy band 0.5–6.0 keV. The image was smoothed for aesthetic purposes via a convolution with a two-dimensional Gaussian function (with $\sigma = 1\farcs1$). The resultant X-ray image can be seen in panel (d) of Figure 1.

Source detection was performed both with the wavdetect tool provided with the CIAO software[4] and by visual inspection of a Gaussian-smoothed image. Our wavdetect analysis was performed on images approximately 63″ on a side (128 × 128 pixels) in the 0.3–8 keV and 0.5–6 keV bandpasses. We used a $\sqrt{2}$ progression for the spatial scales parameter (1, 1.414, 2, 2.828, 4, and 5.657 pixels), and set the detection threshold to 6×10^{-5}, which is approximately the inverse number of pixels in the image; this setting is recommended in the wavdetect help pages to produce only one false positive.

In total, nine statistically significant candidate sources around the ring were found, in addition to a nuclear source in the intruder galaxy, a background quasar, and a foreground star in the vicinity of Arp 147. Light curves and spectra, as well as spectral response files (ancillary response files and redistribution matrix files) and background spectra, were extracted for each candidate source with the ACIS Extract package (AE; Broos et al. 2010). Background spectra were extracted from source-free annular regions around each source and were required to have at least 150 counts in the 0.5–8 keV band. The light curves were examined for variability, but nothing significant was found. Source positions were refined in AE by using the mean photon position as the best estimate of the source's true location. The uncertainty in each source's net counts was calculated using the method of Kraft et al. (1991). Source positions and net counts are listed in Table 1.

The source and background spectra were analyzed with Sherpa 4.2 (Freeman et al. 2001). AE was used to combine each source's spectrum and response files from both ObsIDs. In all of the analyses, the unbinned spectra in the 0.5–8 keV range were fit using the CSTAT statistic, a slight modification of the Cash (1979) statistic, and using the Nelder–Mead optimization algorithm (Nelder & Mead 1965). First, the background spectrum for each source was fit with an absorbed power-law model. Then, the source spectrum was fit with an absorbed power-law model plus a background component based on the background spectrum fit. In all cases, the source spectrum had so few counts that the column density was frozen at the Galactic value in the direction of Arp 147[5] of 6.2×10^{20} cm^{-2}. The unabsorbed fluxes and luminosities are reported in Table 1. The confidence intervals on the fluxes were found by sampling the distribution of power-law parameters 10^4 times and calculating the unabsorbed flux from each set of sampled parameters (the samples of the power-law index were restricted to the range 0–6). The median and standard deviation of the resultant flux distribution are given as the source's flux and uncertainty in Table 1. The power-law index is also reported as a measure of each source's spectral shape. Finally, we also list in Table 1 the median photon energy which, while somewhat instrument-dependent, yields a more statistically significant intercomparison of spectral hardness among the sources.

2.2. Hubble Space Telescope Observations

HST data obtained from an observation (ID 11902) of Arp 147 made on 2008 October 29 were retrieved from the STScI

[4] http://asc.harvard.edu/ciao/

[5] We note that the use of the Galactic N_H value is likely an underestimate since there may be substantial extinction intrinsic to Arp 147; therefore, the cited values of L_x may be biased downward a small amount due to this systematic effect.

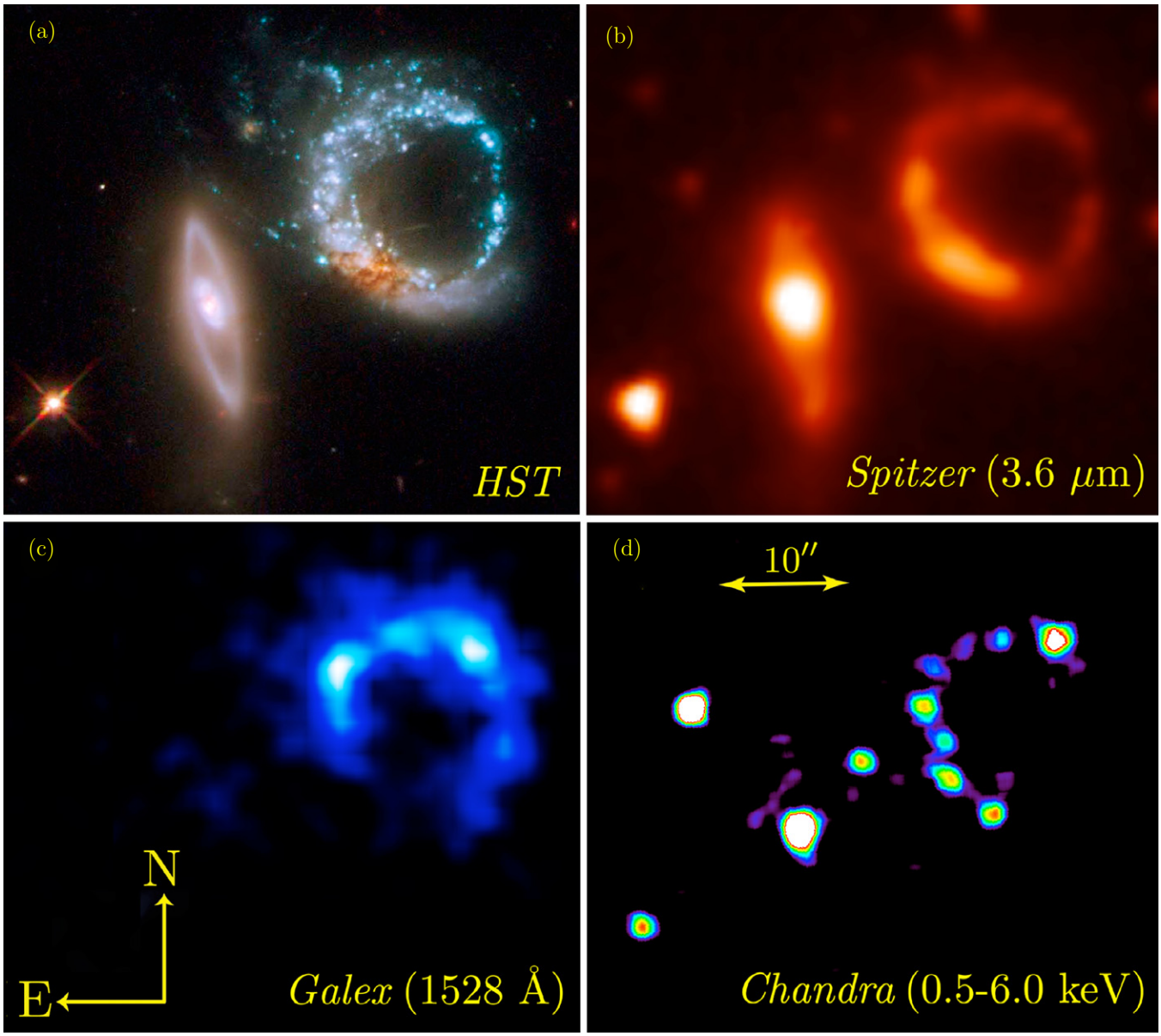

Figure 1. Montage of images taken of the collisional ring galaxy Arp 147. Panel (a): *HST* image taken with WFPC2 (at 4556 Å, 5997 Å, and 8012 Å). Note the intense blue ring associated with star formation as well as the reddish intruder galaxy to the southeast (also exhibiting a ring structure). The blue ring is ∼17″ in diameter, which corresponds to ∼11 kpc at the distance of 133 Mpc. Panel (b): the corresponding *Spitzer* image of Arp 147 in the 3.6 μm band. Panel (c): *Galex* 1516 Å image from archival data. Panel (d): 42 ks *Chandra* image (this work). Aside from eight discrete luminous X-ray sources associated with the ring of star formation, there are four other point sources. From left to right, these correspond to a foreground star, a distant galaxy, the nucleus of the intruder galaxy, and a blue knot that happens to be offset from the main ring.

MAST[6] data archive. High-level science products were provided by the Hubble Heritage Team as part of the Merging and Interacting Galaxies project.[7] The WFPC2 instrument was used for the observation, and exposures were made with the $F450W$ (4556 Å), $F606W$ (5997 Å), and $F814W$ (8012 Å) filters for 8800, 6600, and 6600 s, respectively. The drizzled images had intensity values in counts s^{-1}. We used a large extraction region completely enclosing the Arp 147 ring to determine net count rates of 271, 1095, and 575 counts s^{-1} in the $F450W$, $F606W$, and $F814W$ filters, respectively. Similarly, the intruder galaxy had net count rates of 204, 1230, and 917 counts s^{-1}. These count rates were converted to flux densities (erg cm^{-2} s^{-1} Å^{-1}) using the PHOTFLAM conversion factor found in the header of each FITS image, which was 9.02×10^{-18} for the $F450W$ image, 1.90×10^{-18} for the $F606W$ image, and 2.51×10^{-18} for the $F814W$ image.

2.3. Spitzer Observations

A *Spitzer Space Telescope* observation (ID 20369) of Arp 147 was performed on 2005 August 8 with the IRAC instrument. We retrieved from the *Spitzer* archive the 3.6, 4.5, 5.8, and 8.0 μm post-Basic Calibrated Data mosaic images using the *Spitzer* Leopard software.[8] The total exposure time for each wavelength band was 643 s (24 exposures, each of 26.8 s). We also retrieved the 24.0 μm image acquired with the MIPS

[6] http://archive.stsci.edu/
[7] http://archive.stsci.edu/prepds/merggal/
[8] http://ssc.spitzer.caltech.edu/warmmission/propkit/spot/

Table 1
Arp 147 X-ray Source Properties[a]

Source	R.A. J2000 (h:m:s)	Decl. J2000 (°:′:″)	$\Delta\theta$[b] (″)	Net Counts (0.5–8 keV)	Power-law Photon Index	Median Energy (keV)	F_x[c] (0.5–8 keV)	L_x[d] (0.5–8 keV)
Ring 1	03:11:18.04	+01:19:02.3	0.10	$14.7^{+4.2}_{-3.5}$	$2.0^{+0.5}_{-0.5}$	1.34 ± 0.23	$2.9^{+1.3}_{-0.9}$	$6.2^{+2.8}_{-1.9}$
Ring 2	03:11:18.34	+01:19:02.4	0.15	$6.7^{+3.0}_{-2.3}$	$2.2^{+0.7}_{-0.9}$	1.04 ± 0.36	$1.3^{+1.1}_{-0.6}$	$2.7^{+2.4}_{-1.3}$
Ring 3	03:11:18.57	+01:19:02.0	0.22	$2.7^{+2.1}_{-1.4}$	$1.5^{+1.0}_{-1.0}$	1.82 ± 0.60	$0.68^{+0.9}_{-0.4}$	$1.4^{+1.8}_{-0.8}$
Ring 4	03:11:18.69	+01:19:00.8	0.20	$3.7^{+2.4}_{-1.7}$	$2.5^{+1.0}_{-1.1}$	1.25 ± 0.50	$0.76^{+0.9}_{-0.4}$	$1.6^{+1.9}_{-0.9}$
Ring 5	03:11:18.80	+01:18:57.7	0.14	$7.4^{+3.2}_{-2.5}$	$0.6^{+0.7}_{-0.6}$	1.01 ± 0.36	$2.4^{+1.7}_{-1.0}$	$5.1^{+3.6}_{-2.1}$
Ring 6	03:11:18.66	+01:18:54.4	0.18	$4.5^{+2.6}_{-1.9}$	$2.4^{+0.9}_{-1.0}$	1.35 ± 0.48	$0.9^{+0.9}_{-0.5}$	$1.9^{+2.0}_{-1.0}$
Ring 7	03:11:18.69	+01:18:51.5	0.11	$10.6^{+3.7}_{-3.0}$	$0.9^{+0.5}_{-0.5}$	1.70 ± 0.29	$3.2^{+2}_{-1.2}$	$6.9^{+4.2}_{-2.6}$
Ring 8	03:11:18.47	+01:18:48.2	0.11	$11.7^{+3.8}_{-3.1}$	$1.2^{+0.5}_{-0.5}$	1.41 ± 0.28	$3.2^{+1.8}_{-1.2}$	$6.7^{+3.9}_{-2.5}$
Ring 9	03:11:19.14	+01:18:53.6	0.12	$10.5^{+3.7}_{-3.0}$	$1.3^{+0.5}_{-0.5}$	1.75 ± 0.29	$2.7^{+1.7}_{-1.0}$	$5.7^{+3.6}_{-2.2}$
Galaxy	03:11:19.51	+01:18:48.4	0.06	$41.7^{+6.8}_{-6.1}$	$2.9^{+0.3}_{-0.3}$	0.97 ± 0.13	$6.8^{+1.2}_{-1.0}$	14^{+3}_{-2}
Quasar	03:11:20.05	+01:18:58.9	0.05	$68.7^{+8.6}_{-7.9}$	$1.4^{+0.2}_{-0.2}$	1.48 ± 0.09	$17^{+3.0}_{-2.5}$	NA
Star	03:11:20.41	+01:18:41.7	0.11	$12.6^{+4.0}_{-3.3}$	$2.1^{+0.5}_{-0.6}$	1.22 ± 0.25	$2.5^{+1.2}_{-0.8}$	NA

Notes.
[a] All confidence intervals are 1σ.
[b] $\Delta\theta$ is the relative uncertainty in the source location.
[c] Units for the unabsorbed X-ray flux, F_x, are 10^{-15} erg cm^{-2} s^{-1}.
[d] Units for the unabsorbed X-ray luminosity, L_x, are 10^{39} erg s^{-1}.

instrument on 2006 February 20, which had a total exposure time of 420 s (42 exposures, each 9.96 s). Both the IRAC and MIPS FITS files had pixel values in units of MJy sr^{-1}. The 3.6 μm IRAC image is shown in panel (b) of Figure 1. We converted the images to units of MJy pixel^{-1} based on the pixel sizes of 0.″6012 for the IRAC images and 2.″45 for the MIPS image. We found net flux densities for the Arp 147 ring of 3.8, 2.8, 8.7, 27.5, and 58.8 mJy for the 3.6, 4.5, 5.8, 8.0, and 24 μm images, respectively. Likewise, we found net flux densities for the intruder of 5.4, 3.5, 3.6, 5.3, and 7.3 mJy.

These *Spitzer* spectral points are summarized in Figure 3 as spectral luminosities.

2.4. Galex Observations

We used GalexView 1.4[9] to retrieve data from the *Galex* archive. Tile 181 of the All-Sky Imaging Survey (AIS 181) contains image data on Arp 147 in the near-UV (1771–2831 Å) and far-UV (1344–1786 Å) bands. These bands have effective bandwidths of 732 Å (NUV) and 268 Å (FUV) and effective wavelengths of 2267 Å and 1516 Å. The observation occurred on 2007 October 20 and had an exposure of 216 s in each band. We used the count maps in both bands and defined a 30″ radius circular region to extract the counts from both the Arp 147 ring and the intruder galaxy, which are not completely separated by the *Galex* angular resolution. We used a source-free annulus with inner radius 45″ and outer radius 120″ for our background estimate.

In the NUV image, the net counts from the 30″ inner region are 2603 ± 58, which we attribute to both the ring and the intruder. Using two smaller, non-overlapping elliptical regions (of ∼ 17″ × 21″ and 6″ × 13″ in size), we extracted 2247 ± 50 net counts from the ring and 193 ± 16 net counts from the intruder, respectively. This left 163 net counts unaccounted for. We divided those up proportionally, for a final result of 2397 ± 60 net counts for the ring and 206 ± 20 net counts for the intruder. To estimate the count rate, we took the average value of the NUV relative response high-resolution ("rrhr") map in the vicinity of Arp 147, which was 150 s. The rrhr map combines the relative sensitivity of the detector with the exposure time. Using the conversion factor from count rate to flux density in Table 1.1 of the *Galex* Observer's Guide of 2.05×10^{-16}(erg cm^{-2} s^{-1} Å^{-1})/(counts s^{-1}), we calculate a flux density of $(3.3 \pm 0.08) \times 10^{-15}$ erg cm^{-2} s^{-1} Å^{-1} for the ring and $(2.9 \pm 0.21) \times 10^{-16}$ erg cm^{-2} s^{-1} Å^{-1} for the intruder.

For the FUV image, we follow the same procedure. The net counts from the 30″ inner region are 795 ± 31, which we attribute to both the ring and the intruder. Using two smaller, non-overlapping elliptical regions, we extracted 722 ± 28 net counts from the ring and 36.5 ± 7.0 net counts from the intruder. This left 37 net counts unaccounted for. We divided those up proportionally, for a final result of 757 ± 29 net counts for the ring and 38 ± 9 net counts for the intruder. To estimate the count rate, we took the average value of the FUV "rrhr" map in the vicinity of Arp 147, which was 181.4 s. Using the conversion factor from count rate to flux density in Table 1.1 of the *Galex* Observer's Guide of 1.40×10^{-15}(erg cm^{-2} s^{-1} Å^{-1})/(counts s^{-1}), we calculate a flux density of $(5.8 \pm 0.2) \times 10^{-15}$ erg cm^{-2} s^{-1} Å^{-1} for the ring and $(3 \pm 0.7) \times 10^{-16}$ erg cm^{-2} s^{-1} Å^{-1} for the intruder.

The spectral luminosities from both the ring and the intruder galaxy in the NUV and the FUV are shown in Figure 3.

The FUV image, which has been smoothed via convolution with a two-dimensional Gaussian function (with $\sigma = 0.''7$) for aesthetic purposes, can be seen in panel (c) of Figure 1.

3. RESULTS FROM THE X-RAY OBSERVATIONS

In the *Chandra* image shown in Figure 1(d), we find eight discrete sources at locations around the blue ring plus a source just outside the ring that falls close to or in a blue knot that must be associated with the ring. A bright source is found within ∼1/2″ of the nucleus of the intruder galaxy and two other sources are present at the locations of a bright foreground star and a faint background object. The latter two sources were

[9] http://galex.stsci.edu/galexview

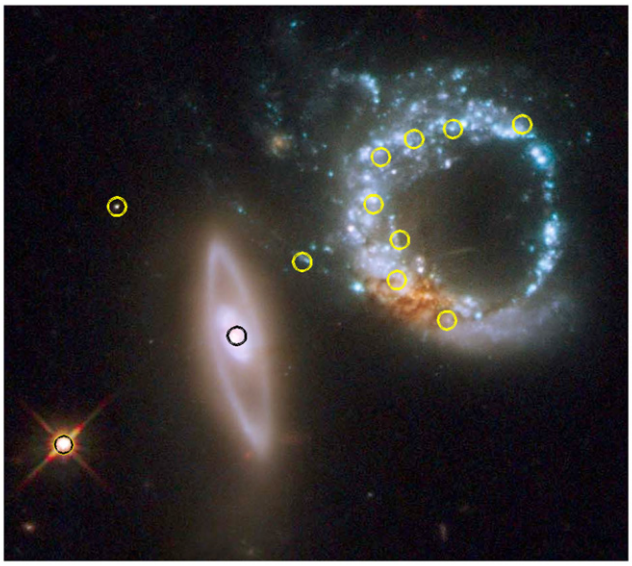

Figure 2. *HST* image of the Arp 147 region with the locations of 12 detected X-ray sources marked with circles. The foreground star to the lower left in the image, and the more distant (point-like) galaxy above it, were used to tie the *Chandra* locations to the *HST* image. We estimate that the resultant astrometric alignment is probably good to between $1/3''$ and $1/2''$, or roughly half the radius of the circles. The alignment between the two images is clearly good enough to show a strong correlation between the blue regions of star formation and the X-ray sources, but insufficiently precise to pinpoint an association between a given X-ray source and a particular blue knot.

used to align the X-ray and optical images to an accuracy of $\sim 1/2''$. The properties of the X-ray sources are summarized in Table 1 (see Section 2.1 for details). The locations of the X-ray sources are shown superposed on the *HST* image in Figure 2.

The faint background source is a 22nd magnitude object identified in the *SDSS* archive as a galaxy (SDSS J031120.03+011858.4), but which is very likely a quasar based on its X-ray luminosity.

The foreground star (SDSS J031120.42+011841.4) has $g = 18.3$, $u - g = 2.55$ and $g - r = 1.53$, and is likely a nearby M star (see, e.g., Smolčić et al. 2004).

We have carried out an autocorrelation analysis of the *HST* image of the ring and find that the characteristic size of the blue knots is $\sim 0\farcs6$, i.e., a few hundred parsecs in physical size. This is also approximately the accuracy of our alignment of the X-ray image to the *HST* image. While it is quite obvious that there are a substantial number of ULX-level X-ray sources associated with the ring of star formation, the $\sim 1''$ resolution of the *Chandra* image, the finite sizes of the blue knots in the *HST* image, their abundance, and the finite precision of the X-ray to optical image alignment prevent us from clearly identifying specific blue knots with particular X-ray sources. Therefore, we cannot positively determine whether the X-ray sources lie in or outside of individual knots.

Another issue is whether, in fact, each apparent source represents the emission from a single object or a blend of fainter sources. To address this, we have carried out a Monte Carlo simulation using a generic X-ray source luminosity function taken from Grimm et al. (2003; $dN/dL_x \propto L_x^{-1.7}$). We choose the X-ray source locations according to a uniform probability distribution within an annular region that approximately represents the ring of star formation. Each simulation is designed to produce an image containing the total X-ray flux that is actually observed. The simulated images are then smoothed with the *Chandra* point-spread function, and examined for detectable sources that may be, in fact, composite. Typically no more than one in eight of our detected sources within the ring can be expected to be comprised of multiple discrete sources. We have not, however, studied cases where the locations of X-ray sources are highly correlated.

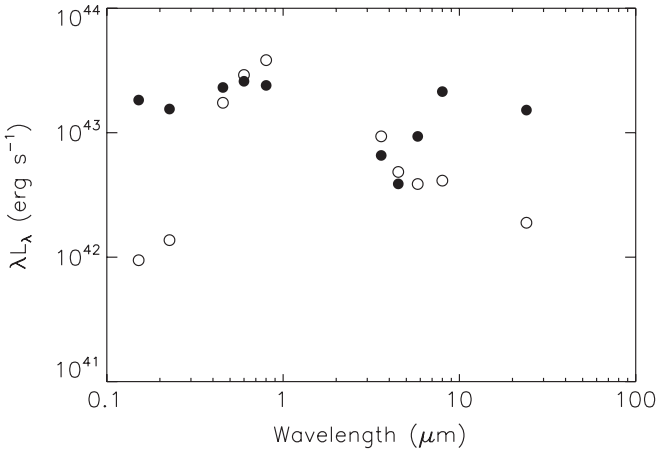

Figure 3. Spectral luminosity distributions (λL_λ) of the integrated light from the entire blue ring of Arp 147 (solid circles) and the entire intruder galaxy (open circles). The points in the UV are from the *Galex* satellite, in the optical from *HST*, and in the IR from *Spitzer*. The λL_λ values for the Arp 147 ring crudely indicate that the spectrum is approximately flat over 2.5 decades in wavelength, and that the total luminosity of the ring (in the 0.1–24 μm band) is $\sim 2 \times 10^{43}$ erg s^{-1}.

4. THE STAR FORMATION RATE

There are a number of empirical relations between spectral fluxes in different bands and star formation rates. Given the excellent wavelength coverage of Arp 147, we attempt to utilize those relations to infer the SFR in the ring and to compare the results from different wavelengths.

A spectral energy distribution, integrated over the entire ring, is shown in Figure 3. Here we have defined $L_\lambda \equiv 4\pi d^2 F_\lambda$, where F_λ is the spectral flux and d is the distance to the source. The quantity λL_λ has the dimensions of luminosity (and is equal to νL_ν). The two UV points are from the *Galex* data, the three visible-region spectral points are from *HST*, and the remaining five IR points are from *Spitzer*.

Infrared spectral intensities at 24 μm and 8 μm can each be used to estimate the SFR (see, e.g., Wu et al. 2005). Equation (1) of Wu et al. (2005) can be written as

$$\mathrm{SFR}(24\ \mu\mathrm{m}) \simeq \frac{\lambda\, L_\lambda}{6.7 \times 10^8\, L_\odot}\ M_\odot\ \mathrm{yr}^{-1}. \qquad (1)$$

The 24 μm flux from the entire Arp 147 ring (see Figure 3) yields an SFR of $\sim 6\ M_\odot\ \mathrm{yr}^{-1}$. Equation (2) of Wu et al. (2005) relates the flux in the 8 μm band to the SFR:

$$\mathrm{SFR}(8\ \mu\mathrm{m}) \simeq \frac{\lambda\, L_\lambda}{1.4 \times 10^9\, L_\odot}\ M_\odot\ \mathrm{yr}^{-1}. \qquad (2)$$

Thus, the 8 μm flux from the entire Arp 147 ring (see Figure 3) yields an SFR of $\sim 4\ M_\odot\ \mathrm{yr}^{-1}$.

The SFR can be estimated from the UV flux by using Equation (12) of Rosa-Gonzalez et al. (2002):

$$\mathrm{SFR}(2000\ \text{Å}) \simeq 6.4 \times 10^{-28}\ \frac{\lambda L_\lambda}{\nu\ (\mathrm{Hz})}\ M_\odot\ \mathrm{yr}^{-1}. \qquad (3)$$

The approximate SFR from the *GALEX* measurement of the near-UV for the Arp 147 ring is $\sim 6\ M_\odot\ \mathrm{yr}^{-1}$, in very reasonable agreement with the values obtained from the *Spitzer* measurements.

Finally, we can use the relationship between the number of luminous X-ray sources (i.e., with $L_x \gtrsim 2 \times 10^{38}$ erg s^{-1}) and SFR given by Grimm et al. (2003), in particular, their Equation (20), to estimate the SFR:

$$\mathrm{SFR} \simeq 0.34 N(L > 2 \times 10^{38}\ \mathrm{erg\ s^{-1}}). \quad (4)$$

The approximate SFR as inferred from the number of luminous *Chandra* X-ray sources in Arp 147 (with $L_x \gtrsim 1.4 \times 10^{39}$ erg s^{-1}) is $\sim 12\ M_\odot\ \mathrm{yr}^{-1}$. This takes into account the fact that the current observations were only sensitive to sources a factor of about 7 more luminous than the Grimm et al. (2003) threshold luminosity, and an assumed differential luminosity function $\propto L^{-1.7}$ (as discussed in Section 3). We can also utilize the analogous expression given by Mapelli et al. (2010):

$$\mathrm{SFR} \simeq 0.83 \pm 0.11 N(L > 10^{39}\ \mathrm{erg\ s^{-1}}). \quad (5)$$

to infer an SFR of $\sim 9\ M_\odot\ \mathrm{yr}^{-1}$, again taking into account the actual lower limit of our luminosity sensitivity.

In any case, all the indicators point to a vigorous SFR within the ring of Arp 147 consistent with $\sim 7\ M_\odot\ \mathrm{yr}^{-1}$. By comparison, the SFR of the Milky Way, which is presumably substantially more massive than the ring ($\sim 8 \times 10^{11}\ M_\odot$ (to within a factor of ~ 1.5) versus $\sim 1.8 \times 10^{11}\ M_\odot$; Battaglia et al. 2006; Gnedin et al. 2010), is $\sim 4 \pm 1\ M_\odot\ \mathrm{yr}^{-1}$ (see, e.g., McKee & Williams 1997; Diehl et al. 2007, and references therein). Nonetheless, it is worth noting that the Milky Way, on the basis of SFR alone, might be expected to host at least several ULXs, but it has at most one (possibly in the form of GRS 1915+105.) To the extent that this is statistically significant, it would imply that something more than just the SFR is involved (e.g., the rate of formation of massive stars, or the metallicity of the galaxy—see Section 5) in determining the number of ULXs present in a particular galaxy.

5. DISCUSSION AND SUMMARY

Arp 147 is a visually impressive pair of galaxies that show the effects of a recent collision. The collision drew the less massive, more gas-rich galaxy into a shape that appears ring-like, at least in projection, and triggered large rates of star formation. A dust-rich region on the south–southeast side of the ring is likely to have evolved from the nuclear region of the original gas-rich galaxy. The intruder galaxy is much redder in color and has a distinct ring structure surrounding a bright nuclear bulge. It seems reasonable to assume that this ring was also induced by the collision. Both the color of the intruder galaxy and the absence of indicators of star formation in its ring suggest that this galaxy was gas poor at the time of the collision.

There are significant uncertainties regarding the geometry and time scales of the collision even though there have been attempts, such as those of Gerber et al. (1992) and Mapelli et al. (2008), to model the event through numerical simulations. Nonetheless, the observed radial velocities and projected separation of the two galaxies suggest the scales of the important parameters. In particular, the recession velocities of the two galaxies differ by ~ 250 km s^{-1}, a difference that may be taken to be loosely representative of the relative velocity projected perpendicular to the line of sight. Since the nucleus of the intruder is separated (in projection) by ~ 10 kpc from the original nucleus of the ring, a relative speed of ~ 250 km s^{-1} would then imply that closest approach occurred ~ 40 Myr ago.

For a Gaussian speed distribution, it is straightforward to show that, given a radial speed, v_r, the probability distribution for the tangential (i.e., sky plane) component, v_t is

$$p(v_t) \propto v_t \sqrt{v_t^2 + v_r^2}\ \exp\left[-\left(v_t^2 + v_r^2\right)/2\sigma^2 \right], \quad (6)$$

where $v_r \simeq 250$ km s^{-1} and we adopt a value of $\sigma \simeq 235$ km s^{-1} (see, e.g., Peebles 1980) since Arp 147 appears not to be part of any significant galaxy group.[10] The most probable (relative) tangential velocity of Arp 147 based on the above probability distribution is ~ 300 km s^{-1}, and the 80% confidence upper and lower limits on v_t are ~ 475 km s^{-1} and ~ 200 km s^{-1}, respectively.

At the former transverse speed, the time since closest approach was at least 20 Myr ago, but the latter transverse speed would imply a time as long as 50 Myr. Since the collision is presumed to be off-center, the shocks in the ISM of the ring may have taken up to ~ 10 Myr to fully develop and lead to copious star formation (M. Krumholz 2010, private communication). Thus, the major epoch of star formation in the ring of Arp 147 likely occurred some 10–40 Myr ago.

We have utilized available multiwavelength images of Arp 147 in the NIR, optical, and UV, as well as new X-ray observations to better understand the star formation and collision history of this interacting pair of galaxies.

The blue ring is luminous in the NIR, optical, UV, and X-ray bands, although its appearance changes in important ways from band to band. A spatially integrated spectrum of the ring is shown in Figure 3. The λL_λ luminosity spectrum is roughly flat over the entire 0.16–24 μm wavelength range (i.e., constant to within a factor of ~ 2). The NIR emission is likely a manifestation of star formation via heating of embedded dust by stellar UV (see Section 4). The brightest NIR emission from the ring comes from near the original nucleus whose reddish color in the *HST* image indicates an abundance of interstellar dust. The ring is lit up in the UV nearly everywhere—except in the vicinity of the original nuclear site where it may be extinguished by dust. It is quite blue in the optical—this is consistent with the detection in the UV. Finally, the luminous X-ray sources are distributed mostly around the northern and eastern parts of the ring which also contain most of the bright blue knots of star formation.

The intruder galaxy is quite bright in the optical and NIR up to ~ 5.8 μm, but then fades at the longer wavelengths (see Figure 3). The *Galex* image of the intruder shows little detectable UV radiation. The integrated spectrum of the intruder is summarized in Figure 3. If we utilize the expressions given in Section 4 that relate the spectral luminosities at 0.2, 8, and 24 μm to the SFR, we find that the intruder has an SFR that is about an order of magnitude lower than that of the ring. We interpret the bright NIR emission of the intruder as being due to dust and polycyclic aromatic hydrocarbons that are heated by ordinary star light (see, e.g., Draine & Li 2007) as well as being due to direct starlight. There is also a luminous X-ray source which we associate with the nucleus of the intruder galaxy. Its luminosity of 1.4×10^{40} erg s^{-1} is in the ULX range, but there is

[10] A $13' \times 13'$ box centered on the SDSS image of Arp 147 (corresponding to a 1 Mpc square) contains only two galaxies that are fainter but of comparable brightness.

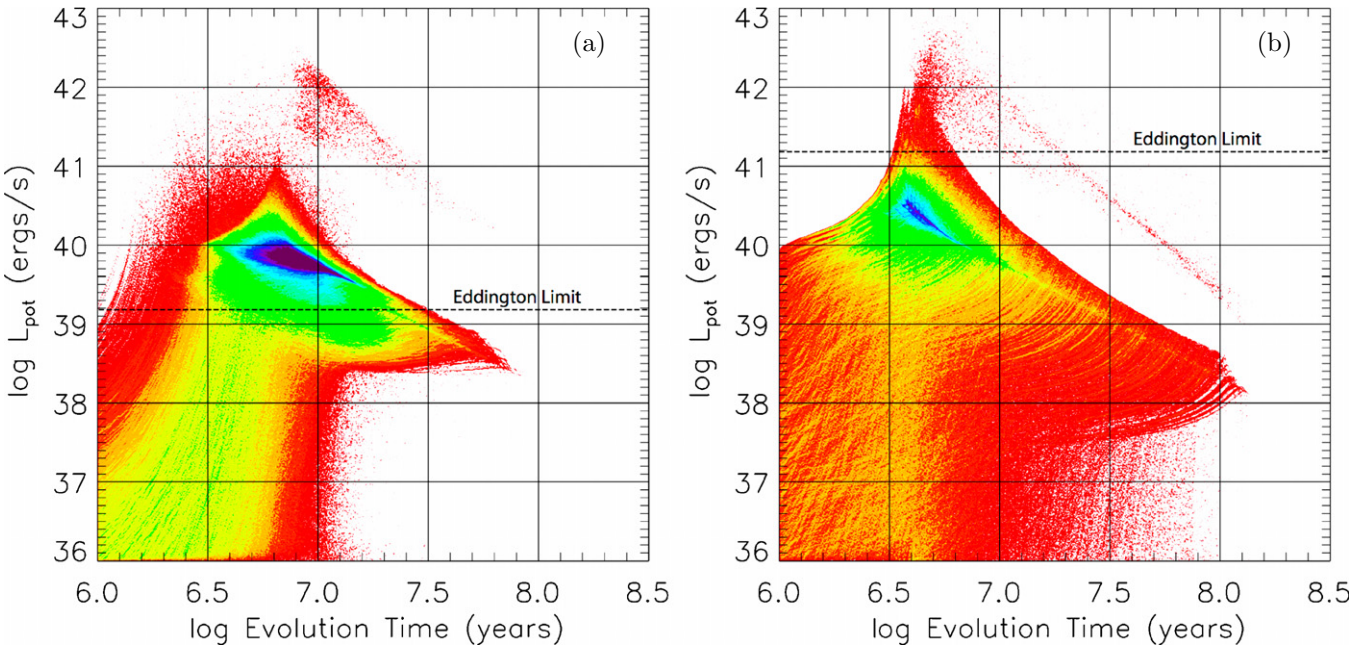

Figure 4. Population synthesis of ULX binaries (adapted from Madhusudhan et al. 2008). Left panel: black-hole accretors with masses in the range of 6–24 $M_\odot$ and donor stars of initial mass 10–34 $M_\odot$. Right panel: IMBH accretors (1000 $M_\odot$) donor stars of initial mass 5–50 $M_\odot$. The plot comprises the evolution tracks of 30,000 binary systems; all assumed to be born during the same starburst event. "Potential" X-ray luminosity is plotted against evolution time (time since the starburst). The potential luminosity is defined to be $L_{\rm pot} = \eta \dot{M} c^2$, where $\dot{M}$ is the mass transfer rate and η is the efficiency of the conversion of rest mass to energy of the accreted material. During the evolution calculations, any mass that is transferred in excess of the Eddington limit is ejected from the system. The potential luminosity is shown here to illustrate how high the luminosity might reach in the absence of the Eddington limit. In panel (a) (panel (b)), the line marked "Eddington Limit" is for a 10 $M_\odot$ (1000 $M_\odot$) black hole accreting H-rich material. The color shading is related to the number of systems at a given evolution time having a given luminosity—blue being maximum and red being minimum, in the ratio of ∼200:1. Very few X-ray sources with $L_x \gtrsim 10^{40}$ erg s^{-1} ($L_x \gtrsim 10^{39}$ erg s^{-1}) remain after ∼15 Myr (45 Myr).

insufficient angular resolution to tell whether this source is truly nuclear or sufficiently off the nucleus to qualify as a ULX. The exact dynamical center of the nucleus of the intruder is difficult to define to better than ∼0.″25 (∼150 pc) due to its irregular shape.

The X-ray luminosities of the nine detected X-ray sources in the ring galaxy are in the range (1.4–7) × 10^{39} erg s^{-1}. At least seven and possibly all of these sources qualify as ULXs (depending on the lower luminosity limit that qualifies as a ULX; see, e.g., Irwin et al. 2004), but none has a luminosity that exceeds 10^{40} erg s^{-1}. In contrast, 9 sources of the 21 detected in the *Chandra* image of the main ring of the Cartwheel galaxy (Gao et al. 2003; Wolter et al. 2006) have L_x in excess of 10^{40} erg s^{-1} even though the distance of the Cartwheel is comparable to that of Arp 147 and the image of the Cartwheel was obtained in a 75 ks exposure. The Cartwheel has a reported SFR of 20 $M_\odot$ yr^{-1} (Mapelli et al. 2010), compared to our finding of ∼7 $M_\odot$ yr^{-1} for Arp 147. Simply scaling by the relative SFRs, we might expect three sources in Arp 147 with L_x in excess of 10^{40} erg s^{-1}, while none is seen. Notwithstanding the small number statistics of the luminous X-ray sources in the Arp 147 blue ring, the absence of high-end ULXs there is plausibly significant relative to the number seen in the Cartwheel.

The difference in the relative numbers of sources with $L_x \gtrsim 10^{40}$ erg s^{-1} suggests a difference in the star formation histories of these galaxies. In the Cartwheel, it appears that a shock wave is moving radially outward in the disk, and star formation has occurred over a long interval (i.e., hundreds of Myr) along or just behind the leading edge of the wave and is still ongoing at present. By contrast, we argue below that the absence of extremely luminous X-ray sources in Arp 147 may indicate that the peak of star formation therein occurred some tens of Myr in the past and has declined sharply as of ∼15 Myr ago. Another possible difference may be the metallicities of the two galaxies. The Cartwheel has $Z \simeq 0.14\, Z_\odot$ and this may well enhance the formation rate of massive, but not IMBH, black holes (see, e.g., Mapelli et al. 2009, 2010). We are unaware of any metallicity determinations for Arp 147.

ULXs are likely to evolve significantly on time scales of millions to tens of millions of years. This is demonstrated in Figure 4, which shows a sample of the results of the population synthesis study of candidate ULXs carried out by Madhusudhan et al. (2008; see also Portegies Zwart et al. 2004b for a related earlier study). The candidate ULXs were (1) conventional high-mass X-ray binaries consisting of a massive donor star initially of mass 10–34 $M_\odot$ and an accreting stellar-mass, i.e., 6–24 $M_\odot$, black hole, and (2) donor stars initially of mass 5–50 $M_\odot$ feeding a 1000 $M_\odot$ black hole (IMBH). All systems were assumed to be born at the same time during a starburst event. In Figure 4, the "potential" X-ray luminosity (see the caption for the definition) is plotted against evolution time (time since the starburst).[11] The color shading is related to the number of systems at a given age (i.e., evolution time) having a given luminosity. Some 30,000 binary evolution tracks are included in each set of simulations.

The simulations of IMBH ULXs show X-ray luminosities that reach or exceed 10^{40} erg s^{-1} for only about 15 Myr. Few ULXs remain after ∼30 Myr. The simulations of accreting stellar mass

[11] We also indicate in Figure 4 the location of the typical Eddington luminosities. In the case of the stellar-mass black hole accretors, we illustrate $L_{\rm Edd}$ for a 10 $M_\odot$ black hole accreting H-rich material. A 20 $M_\odot$ black hole accreting He-rich material (later in the binary evolution) would have $L_{\rm Edd}$ of ∼5 × 10^{39} erg s^{-1}.

black holes yield similar conclusions assuming that either the Eddington limit is not effective, or that the emission can be rather anisotropic, i.e., beamed.

When compared with the maximum luminosities of the X-ray sources in the ring of Arp 147, the simulation results suggest that the SFR in the ring has not been high enough during the past ∼15 Myr to produce ULXs with $L_x \gtrsim 10^{40}$ erg s^{-1}. This is consistent with the inferred time since the collision. This also suggests that the geometry is not like that of the Cartwheel. Rather than a disk with a propagating ring of star formation, Arp 147 is likely a small, tidally elongated and twisted galaxy that does not have such a radially propagating ring of star formation. Measurements of radial velocities at a number of positions around the ring would help to understand the true geometry.

We thank Philip Appleton and Mark Krumholz for helpful discussions. We acknowledge *Chandra* grant GO0-11107X for partial support of this work.

REFERENCES

Amram, P., Mendes de Oliveira, C., Boulesteix, J., & Balkowski, C. 1998, A&A, 330, 881
Appleton, P. N., & Struck, C. 1996, Fundam. Cosm. Phys., 16, 111
Arp, H. C. 1966, ApJS, 14, 1
Arp, H. C., & Madore, B. F. 1987, Catalogue of Southern Peculiar Galaxies and Associations (Cambridge: Cambridge Univ. Press)
Battaglia, G., et al. 2006, MNRAS, 370, 1055
Broos, P. S., Townsley, L. K., Feigelson, E. D., Getman, K. V., Bauer, F. E., & Garmire, G. P. 2010, ApJ, 714, 1582
Cash, W. 1979, ApJ, 228, 939
Colbert, E. J. M., & Mushotzky, R. F. 1999, ApJ, 519, 89
Diehl, R., et al. 2007, in The Obscured Universe, Proc. VI INTEGRAL Workshop, ed. S. Grebenev, R. Sunyaev, & C. Winkler (ESA SP-622; Noordwijk: ESA), 71
Draine, B. T., & Li, A. 2007, ApJ, 657, 810
Fabbiano, G. 2006, ARA&A, 44, 323
Farrell, S. A., Webb, N. A., Barret, D., Godet, O., & Rodrigues, J. M. 2009, Nature, 460, 73
Freeman, P., Doe, S., & Siemiginowska, A. 2001, Proc. SPIE, 4477, 76
Freedman, W. 2003, Am. Sci., 91, 36
Gao, Y., Wang, Q. D., Appleton, P. N., & Lucas, R. A. 2003, ApJ, 596, L171
Gerber, R. A., Lamb, S. A., & Balsara, D. S. 1992, ApJ, 399, L51
Gnedin, O. Y., Brown, W. R., Geller, M. J., & Kenyon, S. 2010, ApJ, 720, L108
Godet, O., Barret, D., Webb, N. A., Farrell, S. A., & Gehrels, N. 2009, ApJ, 705, L109
Grimm, H.-J., Gilfanov, M., & Sunyaev, R. 2003, MNRAS, 339, 793
Higdon, J. L. 1995, ApJ, 455, 524
Irwin, J. A., Bregman, J. N., & Athey, A. E. 2004, ApJ, 601, L143
King, A. R. 2004, MNRAS, 347, L18
Kraft, R. P., Burrows, D. N., & Nousek, J. A. 1991, ApJ, 374, 344
Krolik, J. H. 2004, ApJ, 615, 383
Lynds, R., & Toomre, A. 1976, ApJ, 209, 382
Madhusudhan, N., Rappaport, S., Podsiadlowski, Ph., & Nelson, L. 2008, ApJ, 688, 1235
Madore, B. F., Nelson, E., & Petrillo, K. 2009, ApJS, 181, 572
Mapelli, M., Colpi, & Zampieri, L. 2009, MNRAS, 395, 71
Mapelli, M., Moore, B., Giordano, L., Mayer, L., Colpi, M., Ripamonti, E., & Callegari, S. 2008, MNRAS, 383, 230
Mapelli, M., Ripamonti, E., Zampieri, L., Colpi, M., & Bressan, A. 2010, MNRAS, in press (arXiv:1005.3548)
McKee, C. F., & Williams, J. P. 1997, ApJ, 476, 144
Mihos, J. C., & Hernquist, L. 1994, ApJ, 437, 611
Nelder, J. A., & Mead, R. 1965, Comput. J., 7, 308
Peebles, P. J. E. (ed.) 1980, The Large-scale Structure of the Universe (Princeton, NJ: Princeton Univ. Press)
Portegies Zwart, S. F., Baumgardt, H., Hut, P., Makino, J., & McMillan, S. L. W. 2004a, Nature, 428, 724
Portegies Zwart, S. F., Dewi, J., & Maccarone, T. 2004b, MNRAS, 355, 413
Rosa-González, D., Terlevich, E., & Terlevich, R. 2002, MNRAS, 332, 283
Smith, B. J., Struck, C., & Nowak, M. A. 2005, AJ, 129, 1350
Smolčić, V., et al. 2004, ApJ, 615, L141
Toomre, A. 1978, in IAU Symp. 79, The Large-scale Structure of the Universe, ed. M. S. Longair & J. Einasto (Dordrecht: Reidel), 109
Whitmore, B. C., & Schweizer, F. 1995, AJ, 109, 960
Wolter, A., Trinchieri, G., & Colpi, M. 2006, MNRAS, 373, 1627
Wu, H., Cao, C., Hao, C. N., Liu, F.-S., Wang, J.-L., Xia, X.-Y., Deng, Z.-G., & Young, C. K.-S. 2005, ApJ, 632, L79
Yungelson, L. R., van den Heuvel, E. P. J., Vink, J. S., Portegies Zwart, S. F., & de Koter, A. 2008, A&A, 477, 223
Zezas, A., & Fabbiano, G. 2002, ApJ, 577, 726